

# X-ray section only of DoAr 21 paper, Jensen et al.

David H. Cohen<sup>1\*</sup>

<sup>1</sup>*Swarthmore College, Department of Physics and Astronomy, Swarthmore, Pennsylvania 19081, USA*

5 March 2009

## ABSTRACT

*Note: This is simply a draft of the X-ray section of the DoAr 21 paper.*

**1 INTRODUCTION**

**2 STELLAR PROPERTIES**

### 3 X-RAY EMISSION

DoAr 21 is the brightest X-ray source in the  $\rho$  Oph cloud core A, with an X-ray luminosity of nearly  $10^{32}$  ergs  $s^{-1}$   $cm^{-2}$ , a hard thermal spectrum, and large X-ray flares seen in several archival observations at a rate of nearly one per day. Its X-ray emission has been observed at low resolution with *Einstein* (Montmerle et al. 1983), *ASCA* (Casanova et al. 1995), *ROSAT* (Koyama et al. 1994), and *Chandra* (Imanashi et al. 2002; Gagné et al. 2004).

The new *Chandra* grating spectra we present here have vastly superior spectral resolution compared to any of these previous datasets, enabling us to extract temperature and abundance information with more reliability and also, for the first time, to examine density and velocity diagnostics. Given the high rate of flaring seen in previous observations, it is not surprising that we detected a large and well resolved flare in the 91 ksec *Chandra* observation that we present here. We can bring many of these same diagnostic tools to bear on the different portions of the new dataset - pre-flare, flare, and post-flare.

The High Energy Transmission Grating Spectrometer (HETGS) has two grating arrays - the Medium Energy Grating (MEG) with a FWHM resolution of 2.3 mÅ, and the High Energy Grating (HEG) with a resolution of 1.2 mÅ. Both grating arrays operate together, with the dispersed spectra (first, second, and third orders) as well as the zeroth order spectrum recorded on the ACIS CCD array. We used standard CIAO (v.3.3) tools to extract the dispersed spectra (as well as the zeroth order spectrum), and to create observation specific spectral response matrices (rmfs) and effective area tabulations (garfs), as well as to create light curves (and spectra for each of the three subsets of the observation). We analyzed the spectra in XSPEC v.12.3.

The goal of this X-ray spectral and timing analysis is to characterize the properties of the hot plasma on this very magnetically active pre-main-sequence star, and compare its properties to those measured in the handful of other PMS stars with high-resolution X-ray spectra. Its extreme youth and lack of obvious signatures of accretion make for an interesting contrast between DoAr 21 and the strongly accreting T Tauri stars that have been well-studied with the *Chandra* gratings.

Initially, we suspected that DoAr 21 is a transition disk system and that its X-ray properties might lie between those of naked T Tauri stars and young, magnetically active ZAMS stars on the one hand, and classical T Tauri stars, which show soft X-ray emission and altered density-sensitive line ratios that might be indicative of an accretion-based X-ray production mechanism, on the other hand. We now suspect that DoAr 21 is not undergoing any accretion and that the circumstellar material in its vicinity is not in the form of a disk. The observed X-rays, and the unobservable far- and extreme-UV emission associated with the X-ray emitting plasma as it cools, could have an important effect on the circumstellar material, perhaps being the dominant source of excitation for the PAH emission we reported on in the previous section. So, characterizing the X-ray properties of the star are important for understanding the physical conditions in the circumstellar environment, too.

In Fig. 1 we show the MEG and HEG spectra (negative and positive first orders coadded in both cases), with emis-

sion lines identified and labeled. Although the *Chandra* gratings and detector have significant response to wavelengths above 30 Å, interstellar attenuation (due to photoelectric absorption, which has a cross section that goes roughly as  $\lambda^3$ ) makes the spectrum above 12 Å nearly devoid of counts. These spectra are dominated by a strong bremsstrahlung continuum, which is indicative of plasma with a dominant temperature well in excess of 20 million K (so that atoms are mostly fully stripped and their associated line emission is weak). The presence of emission from high ion stages - up to helium-like Fe xxv - also indicates very high plasma temperatures. We analyze the temperature distribution in the plasma in detail, below, both by fitting thermal emission models to the entire spectrum and also by looking at ratios of lines arising from adjacent ionization states of the same element.

A large flare was seen in the middle of the *Chandra* observation, with a rapid rise of just a few 1000 seconds, followed by an exponential decay that also shows evidence for reheating. The temporal behavior is shown in Fig. 2, where we also show light curves for the hard and soft bands separately. Significant hardening is seen during the flare, which persists through the post-flare phase. We will first discuss global fits to the total spectrum collected during the 91 ks observation. We will then discuss fits to separate spectra, formed from the pre-flare (0 through 48 ks) section of the observation, the flare (48 to 70 ks) section, and the post-flare (70 to 91 ks) section. These temporal divisions are indicated by the vertical lines in the top panel of Fig. 2.

We fit the MEG and HEG first order dispersed spectra simultaneously (but not co-added) over the spectral ranges where each had a significant number of counts. For the MEG this was 2 to 12.5 Å, and for the HEG it was 1.5 to 11.5 Å. We fit a two-temperature optically thin thermal emission model (the *bapec* implementation of the Astrophysical Plasma Emission Code (APEC) (Smith et al. 2001)) that accounts for bremsstrahlung and line emission from a plasma in statistical equilibrium. This model has four free parameters: the plasma temperature, the abundances (expressed as a fraction of solar), the emission measure (proportional to the normalization of the model, and formally given by  $4\pi d^2 \int n_e n_H dV$ ), and the line broadening (an ad hoc turbulent velocity added in quadrature to the thermal velocity of each line in the model). We also include interstellar attenuation, with cross sections from Morrison & McCammon (1983). We used the  $\chi^2$  statistic with Churazov weighting to assess goodness of fit and to place confidence limits on the derived model parameters.

*(Co-authors: I must check my records regarding the 2nd and 3rd order spectra as well as any background subtraction I may or may not have done. ...and the formalism of the turbulent broadening in bapec and the cross sections in the wabs model.)*

A single temperature model does not provide a good fit, though the low resolution *ROSAT* and *Chandra* ACIS data, are adequately fit by a single temperature thermal model (Imanashi et al. 2002). We did find a good fit when we used a two temperature *bapec* model with interstellar absorption. The best-fit model has temperatures of roughly 1 and 4 keV, with approximately five times the emission measure in the



**Table 1.** APEC model fits

	$kT_1$ (keV)	$EM_1$ ( $\text{cm}^{-3}$ )	Abund <sub>1</sub>	$kT_2$ (keV)	$EM_2$ ( $\text{cm}^{-3}$ )	Abund <sub>2</sub>	$N_{\text{H}}(ISM)$ ( $\text{cm}^{-2}$ )
total	$1.00^{+0.04}_{-0.03}$	$6.82^{+0.82}_{-0.69} \times 10^{53}$	$0.39 \pm .02$	$4.16 \pm .11$	$3.07^{+0.06}_{-0.07} \times 10^{53}$	$0.39^a$	$1.19^{+0.03}_{-0.04} \times 10^{22}$
pre-flare	$0.95^{+0.05}_{-0.06}$	$7.40^{+1.37}_{-1.19} \times 10^{53}$	$0.26 \pm .02$	$3.10^{+0.14}_{-0.13}$	$2.18^{+0.09}_{-0.11} \times 10^{54}$	0.26	$1.19^{+0.03}_{-0.05} \times 10^{22}$
flare	$1.20^{+0.08}_{-0.10}$	$7.93^{+2.04}_{-1.72} \times 10^{53}$	$0.40^{+0.05}_{-0.04}$	$5.21^{+0.79}_{-0.33}$	$3.22^{+0.15}_{-0.21} \times 10^{54}$	0.40	$1.13^{+0.05}_{-0.04} \times 10^{22}$
post-flare	$0.80^{+0.09}_{-0.05}$	$1.11^{+0.24}_{-0.16} \times 10^{54}$	$0.31^{+0.05}_{-0.04}$	$4.49^{+0.24}_{-0.50}$	$3.69^{+0.21}_{-0.16} \times 10^{54}$	0.31	$1.18^{+0.06}_{-0.05} \times 10^{22}$

<sup>a</sup> If a parameter listed in the table has no uncertainty listed, then its value was not independently fit. In the case of the abundance of the second temperature component, this value was sometimes free to vary, but tied to the abundance of the first temperature component.

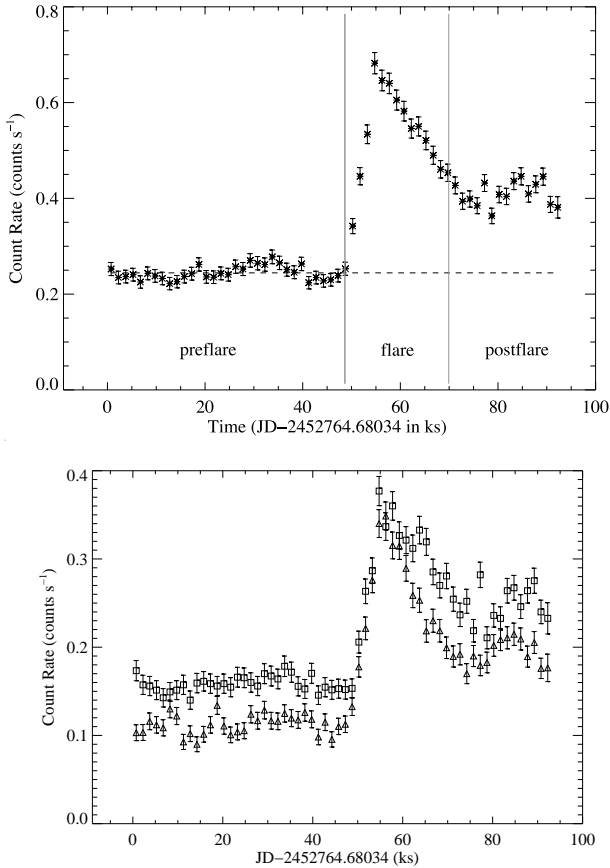


**Figure 2.** A light curve with 1500 second bins, formed from all counts with energies between 0.5 and 8.0 keV in the zeroth order spectrum as well as the dispersed spectra (top). In the bottom panel, we show light curves made from all counts with energies below 2 keV (circles) and above 2 keV (triangles). The hardening of the spectrum during and after the flare is evident.

but we are able to analyze the strengths of several of the strongest ones, and use them as plasma diagnostics. Specifically, the ratios of hydrogen-like to helium-like lines are temperature sensitive, and can be used to augment the temperature information from the global spectral modeling described above. Additionally, the forbidden-to-intercombination line ratios of helium-like ions are sensitive to density, as collisions de-populate the metastable upper level ( $^3S$  of the forbidden line), and populate the upper level  $^3P$  of the intercombina-

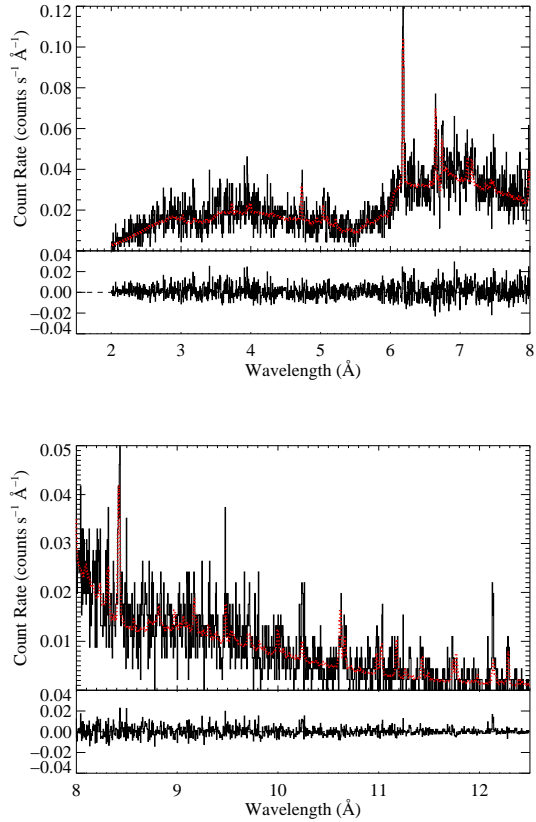


**Figure 3.** The best-fit two-temperature thermal emission model is superimposed (in red) on the MEG data. Fit residuals are shown below each plot.

tion line. Thus high densities (different critical densities for each element) decrease the forbidden-to-intercombination ( $f/i$ ) ratio. This behavior is seen in some accreting T Tauri stars, but not in naked T Tauri or magnetically active main sequence stars.

We measured the line intensities by fitting the continuum near to each line as a flat spectrum, consistent with bremsstrahlung, and once the continuum level was established, we fit the line with a Gaussian profile model on top of the best-fit continuum level. For the closely spaced helium-like complexes, we fit all three lines simultaneously. The Si XIV/XIII and S XVI/XV ratios are  $1.50^{+0.33}_{-0.28}$  and  $0.55^{+0.26}_{-0.13}$ , re-

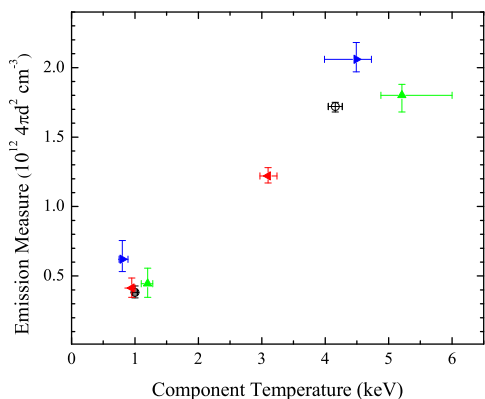


**Figure 4.** Summary of the parameters of the two-temperature fits to the pre-flare, flare, and post-flare data, along with the fits to the entire dataset (open circles).

spectively. For the helium-like intensity we use the flux in the resonance, intercombination, and forbidden lines combined. We modeled the temperature dependence of these line ratios using the collisional-radiative equilibrium code, PrismSpect (ref), and find that the measured values imply temperatures of XX and YY. We also used APEC to model the temperature dependence, and got similar results.

(Co-authors: The temperature modeling still needs to be done. And the results discussed in the context of the 2-T APEC modeling. We will also look at these ratios in the pre-flare, flare, and post-flare spectra, separately.)

The  $f/i$  ratios for Si XIII and S XV are  $5.4_{-2.2}^{+2.6}$  and  $1.90_{-0.82}^{+2.28}$ , respectively. None of the lower atomic number elements have enough signal-to-noise in their helium-like emission complexes for a measurement to be made. For the Si XIII, the ratio exceeds that low-density limit<sup>1</sup> of  $f/i = 2.3$  to 2.5 with one sigma significance. This limits the density to less than  $\sim 10^{12} \text{ cm}^{-3}$ . The 95 percent confidence limit is  $9 \times 10^{12} \text{ cm}^{-3}$ . For S XV the forbidden-to-intercombination ratio is consistent with the low-density limit of  $f/i = 2.0$  to 2.1. The one sigma lower limit on  $f/i$  for S XV corresponds to a density of  $10^{14} \text{ cm}^{-3}$ . The constraints are depicted in Fig. 5 and the HEG measurement of the Si XIII complex – which provides the tightest constraints – is shown in Fig. 6.

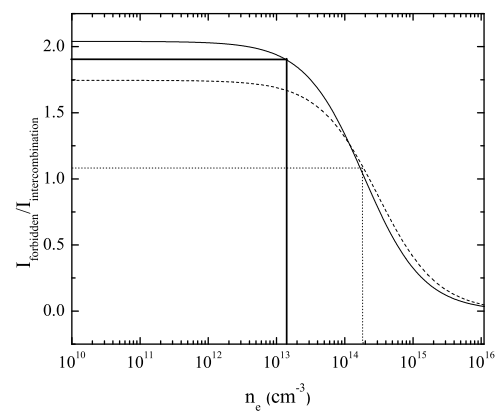
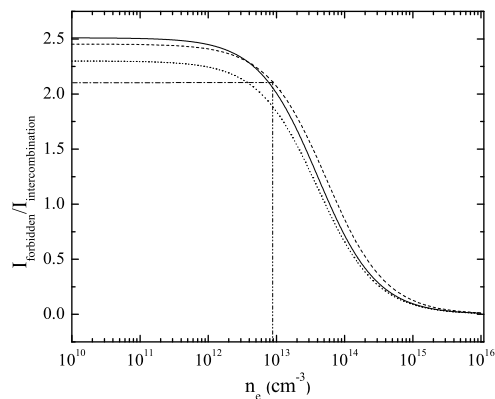


**Figure 5.** Models of the  $f/i$  ratios of Si XIII (top) and S XV (bottom), as a function of electron density. The models are from Blumenthal et al. (1972) (solid curve), Porquet & Dubau (2000) (dotted), and PrismSpect (dashed). In the bottom panel, the solid horizontal line represents the best-fit  $f/i$  value and the solid vertical line represents the corresponding electron density. The dash-dot lines represent the one sigma lower limit on the  $f/i$  ratio and the corresponding upper limit on the electron density. In the top panel we show only the 95 percent lower limit on  $f/i$  of 2.10 as a dash-dot line, corresponding to a 95 percent upper limit on density of  $n_e = 9 \times 10^{12} \text{ cm}^{-3}$ .

<sup>1</sup> The low density limit refers to the density below which collisional excitation out of the metastable excited state of the forbidden line is unimportant compared to spontaneous emission to the ground state. We give a range of values for the low-density  $f/i$  limit for each element. These represent the range of values found from PrismSpect calculations and from Blumenthal et al. (1972) and Porquet & Dubau (2000).

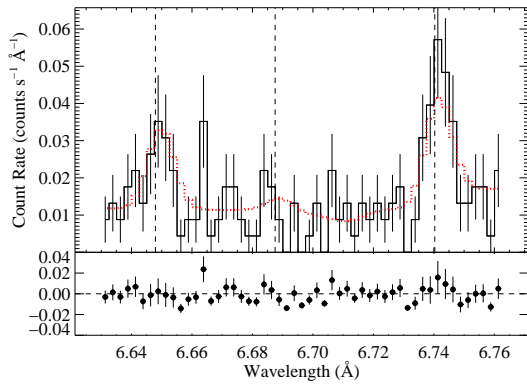


**Figure 6.** The Si XIII in the HEG shows a strong forbidden line (at 6.74 Å) and a weak intercombination line (at 6.68 Å), consistent with the low-density limit. (*Co-authors: should we show any of the other complexes?*)

**REFERENCES**

- Blumenthal G.R., Drake G.W.F., Tucker W.H., 1972, ApJ, 172, 205  
Casanova S., Montmerle T., Feigelson E. D., André P., 1995, ApJ, 439, 752  
Gagné M., Skinner S. L., Daniel K. J., 2004, ApJ, 613, 393  
Imanishi K., Tsujimoto M., Koyama K., 2002, ApJ, 572, 300  
Koyama K., Maeda Y., Ozaki M., Ueno S., Kamata Y., Wawara, Y, Sinner S., Yamauchi S., 1994, PASJ, 46, L125  
Montmerle T., Koch-Miramond L., Falgarone E., Grindlay J. E., 1983, ApJ, 269, 182  
Morrison R., McCammon D., 1983, ApJ, 270, 119  
Porquet D., Dubau J., 2000, A&AS, 143, 495  
Smith R. K., Brickhouse N. S., Liedahl D. A., Raymond J. C., 2001, ApJ, 556, L91